DOI: 10.15480/882.9359

Eighth International Symposium on Marine Propulsors
smp'24, Berlin, Germany, March 2024

Acoustic signature of a wetted propeller in the wake of a hydrofoil

Antonio Posa, Riccardo Broglia, Mario Felli

National Research Council of Italy, Institute of Marine Engineering (CNR-INM), Rome, Italy

ABSTRACT

Data from Large Eddy Simulations (LES) were exploited to compute the acoustic signature of a wetted propeller working in the wake of a hydrofoil at incidence angles of $0\,\mathrm{deg}$, $10\,\mathrm{deg}$ and $20\,\mathrm{deg}$. A computational grid consisting of 1.7 billion points was utilized in the framework of an immersed-boundary (IB) methodology to resolve the fluid dynamics. The Ffowcs-Williams & Hawkings (FWH) acoustic analogy was employed for the computation of the acoustic pressure from the hydrofoil-propeller system in post-processing. The results of the acoustic analysis show that the signature of the propeller is the highest in its upstream and downstream directions, while minima are located on the propeller plane in the direction aligned with the span of the hydrofoil. Also the influence of the incidence angle of the hydrofoil on the acoustic signature of the propeller is analyzed. It is reinforced at large angles, which produce separation phenomena on the suction side of the hydrofoil and enhance the loading component of the sound coming from the propeller blades operating in its wake.

Keywords

Large Eddy Simulation, Ffowcs-Williams & Hawkings acoustic analogy, Immersed Boundaries

1 INTRODUCTION

The prediction of underwater noise from marine propulsion is the subject of a growing interest, due to its detrimental impact on the environment (Chou et al 2021). Although several studies dealing with the acoustic signature of marine propellers are currently available in the literature, their acoustic analysis is usually limited to only a few locations in the vicinity of the propulsion system, which do not provide a full picture of its directivity. To the authors' knowledge, the only exceptions are the recent works by Kimmerl & Abdel-Maksoud (2023), Posa et al (2023a) and Posa et al (2023b), where the acoustic far field is investigated across a large number of positions.

Numerical simulations can provide detailed information on the fluid dynamics and in turn on the hydroacoustics of propulsion systems, for instance through the exploitation of the acoustic analogy (Lighthill1952): since the fluid dynamics is not substantially modified by the acoustic phenomena, it is legitimate to resolve the former without taking into account the latter and then reconstruct the acoustic pressure, by using the database of fluid dynamic solutions of the flow. Of course, the accuracy of the overall approach is tied to the fidelity of the simulations and their ability to resolve a wide range of scales, to cover a wide range of frequencies of the acoustic phenomena. For this reason, eddy-resolving techniques, as Detached Eddy Simulation (DES) and LES, are becoming increasingly popular for the reconstruction of the sound radiated from propellers, coupled with the acoustic analogy. A few examples can be found in the recent works by Bensow & Liefvendahl (2016), Cianferra et al (2019), Kimmerl et al (2021), Lidtke et al (2022), Sezen & Atlar (2022), Stark & Shi (2021), Ge et al (2022), and Posa et al (2022a).

In the present study, results of LES computations, conducted on a cylindrical grid consisting of 1.7 billion points, are utilized to reconstruct the acoustic signature of a hydrofoil-propeller system in wetted conditions, by using the FWH acoustic analogy (Ffowcs-Williams & Hawkings 1969). The acoustic field is computed on a sphere of 64,800 hydrophones, having a radius of 100 propeller diameters and centered at the propeller. The direct formulation of the FWH acoustic analogy allows us to separate the sound from the hydrofoil and the propeller, respectively, in contrast with the more widespread permeable formulation by Di Francescantonio (1997).

Below, this paper is organized as follows. In section 2, the methodologies to resolve both the fluid dynamics and the hydroacoustics are discussed. In section 3, the setup of both fluid dynamic simulations and acoustic post-processing are provided. Section 4 reports the analysis of the acoustic signature of the hydrofoil-propeller system at three particular frequencies. Eventually, section 5 summarizes the results of this study.

2 METHOD

2.1 Solution of the fluid dynamics

The flow problem was tackled by resolving the filtered Navier-Stokes equations (NSEs) for incompressible flows. The subgrid stresses were modeled by using the wall-adaptive local eddy-viscosity model by Nicoud & Ducros (1999). The interaction between the bodies and the flow was handled by means of an IB methodology. This relaxes the requirement of the topology of the Eulerian grid to conform the shape of the bodies immersed within the flow. Therefore, the NSEs were resolved on a cylindrical, Eulerian grid, discretizing the computational domain. The geometry of the bodies was represented by Lagrangian surface grids, which were "immersed" within the Eulerian grid. The relative position between the elements of the Lagrangian grids and the points of the Eulerian grid allowed defining the forcing terms to introduce within the momentum equation to enforce the no-slip requirement of the surface of the bodies. In comparison with conventional, more "traditional" body-fitted methodologies, IB methods do not provide the flexibility of prescribing grid points on the surface of the bodies immersed within the flow. However, besides the substantial advantage of dramatically simplifying the mesh generation process, they allow handing moving bodies without sliding interfaces or other techniques of mesh deformation, which have the critical drawback of producing numerical, spurious noise. More details on the particular IB method can be found in the literature (Balaras 2004).

The NSEs were discretized in space using second-order, centered finite-differences on a staggered cylindrical grid. The advancement in time adopted a fractional-step methodology. The discretization in time along the radial and axial directions utilized the explicit three-step Runge-Kutta scheme, while the implicit Crank-Nicolson scheme was adopted in the azimuthal direction to relax the stability requirements arising at the axis of the cylindrical grid. For efficiency, the hepta-diagonal Poisson problem resulting from the continuity condition was decomposed into a series of penta-diagonal problems by trigonometric transformations along the azimuthal direction. Then, each of them was inverted by using an efficient direct solver. The overall NSEs solver was demonstrated second-order accurate in both space and time on canonical flow problems and was successfully adopted in a series of cases involving marine propellers, including comparisons with experiments, as reported in Posa et al (2019) and Posa et al (2022c).

2.2 Reconstruction of the acoustic signature

The acoustic signature was reconstructed by means of the acoustic analogy, which is based on the hypothesis that the fluid dynamics is not significantly modified by the acoustic phenomena. Therefore, it is possible to resolve the fluid dynamics without taking into account the latter and compute the acoustic pressure in post-processing. This was achieved in the present work by considering the FWH equation in integral form, as below:

$$4\pi\widehat{p}(\boldsymbol{x},t) = \frac{\partial}{\partial t}\int_{\mathbb{S}}\left[\frac{\rho^* v_n}{r|1-\mathbb{M}_r|}\right]_{\mathbb{T}} dS + \frac{1}{c}\frac{\partial}{\partial t}\int_{\mathbb{S}}\left[\frac{p'\widehat{n}_i\widehat{r}_i}{r|1-\mathbb{M}_r|}\right]_{\mathbb{T}} dS + \int_{\mathbb{S}}\left[\frac{p'\widehat{n}_i\widehat{r}_i}{r^2|1-\mathbb{M}_r|}\right]_{\mathbb{T}} dS + \frac{1}{c^2}\frac{\partial^2}{\partial t^2}\int_{\mathbb{V}}\left[\frac{T_{rr}}{r|1-\mathbb{M}_r|}\right]_{\mathbb{T}} dV + \frac{1}{c}\frac{\partial}{\partial t}\int_{\mathbb{V}}\left[\frac{3T_{rr}-T_{kk}}{r^2|1-\mathbb{M}_r|}\right]_{\mathbb{T}} dV + \int_{\mathbb{V}}\left[\frac{3T_{rr}-T_{kk}}{r^3|1-\mathbb{M}_r|}\right]_{\mathbb{T}} dV, \quad (1)$$

where $\widehat{p}$ is the acoustic pressure, $\boldsymbol{x}$ is the position vector of the receiver, t is time, ρ^* is a reference density, taken in this case equal to the density of the fluid, $\rho^* = \rho$, v_n is the velocity component of the elemental surface dS in its normal direction, p' is the time fluctuation of the hydrodynamic pressure, relative to the reference pressure p^*, $\widehat{n}_i$ is the component in the i direction of the unit vector normal to the elemental surface dS, c is the speed of sound in the fluid and $\mathbb{S}$ and $\mathbb{V}$ are the surface and volume of integration. The vector $\boldsymbol{r} = \boldsymbol{x} - \boldsymbol{y}$ represents the position of the receiver, relative to the source of position $\boldsymbol{y}$. Therefore, in Equation 1 the quantity r is the magnitude of the vector $\boldsymbol{r}$, $\widehat{r}_i$ is the component in the direction i of the unit vector of $\boldsymbol{r}$ and $\mathbb{M}_r$ is the Mach number in the direction of $\boldsymbol{r}$. The volume integrals of Equation 1 include the Lighthill tensor:

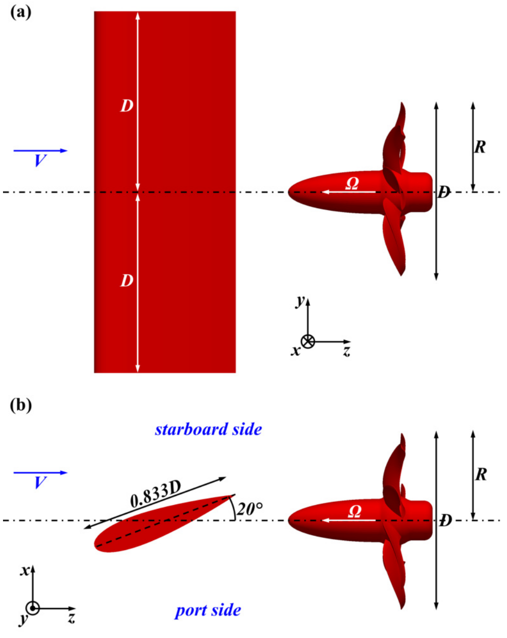

Figure 1: Geometry of the hydrofoil-propeller system in the case of the hydrofoil at 20 degrees incidence: (a) lateral view; (b) top view.

$$T_{ij} = \rho u_i u_j + \left[(p-p^*) - c^2(\rho-\rho^*)\right]\delta_{ij} - \sigma_{ij}, \quad (2)$$

where u_i and u_j are the velocity components in the i and j directions, δ_{ij} is the Kronecker delta, while σ_{ij} is the tensor of the viscous stresses. The quantities T_{rr} and T_{kk} in Equation 1 are respectively $T_{rr} = T_{ij}\widehat{r}_i\widehat{r}_j$ and the trace of the Lighthill tensor.

It is worth mentioning that all integrals at the RHS of Equation 1 should be computed at the emission time, $\mathbb{T}$:

$$\mathbb{T} = t - r/c = t - \frac{|\boldsymbol{x}(t) - \boldsymbol{y}(\mathbb{T})|}{c}. \quad (3)$$

However, since the speed of sound is much higher than the one of the propeller, it is legitimate to assume the time delay r/c negligible. This assumption was verified by literature of the sound from marine propellers, as discussed in detail by Cianferra et al (2019), and allows a substantial simplification of post-processing.

3 SETUP

3.1 Setup of the fluid dynamic simulations

The setup of the computations includes a seven-bladed submarine propeller (INSEAN E1658), working in the wake of a NACA0020 hydrofoil, mimicking a simplified rudder. The spanwise extent of the hydrofoil is equivalent to $2D$, where D is the diameter of the propeller. The chord of the hydrofoil is equivalent to $0.833D$. In its configuration at $0\,\mathrm{deg}$ incidence it is aligned with the axis of the propeller and the streamwise distance between its trailing edge and the propeller plane is equivalent to $0.85D$. Two additional configurations of the system were generated by rotating the hydrofoil of $10\,\mathrm{deg}$ and $20\,\mathrm{deg}$ around its mid chord. These three cases will be indicated below as ***I00***, ***I10*** and ***I20***. The geometry of the system is illustrated in Figure 1 for the case ***I20***. It is worth mentioning that the rotation of the propeller makes the overall system asymmetric, therefore the results at $10\,\mathrm{deg}$ and $20\,\mathrm{deg}$ of incidence of the hydrofoil are not representative of cases at $-10\,\mathrm{deg}$ and $-20\,\mathrm{deg}$. Unfortunately, the substantial computational cost of the adopted approach did not allow extending this study to these additional conditions.

The propeller was simulated at the same working conditions as in Posa et al (2019), where the overall approach was validated against the Particle Imaging Velocimetry experiments by Felli & Falchi (2018), as well as against their dynamometric measurements on global performance. These conditions are represented by the following values of advance coefficient and Reynolds number:

$$J = V/nD = 0.65, \tag{4}$$

$$Re = b_{70\%R}\sqrt{(2\pi n\ 0.7R)^2 + V^2}/\nu = 310{,}000, \tag{5}$$

where V is the advance velocity, n is the frequency of the rotation of the propeller, $b_{70\%R}$ is the chord of the propeller blades at 70% of the radial extent of the propeller, R, and ν is the kinematic viscosity of the fluid.

The problem was simulated within a cylindrical domain, having a radial extent equal to $5D$ and spanning a length of $5D$ both upstream and downstream of the propeller plane. At the inflow boundary, uniform conditions of unit streamwise velocity were enforced, while at the outflow, convective conditions were utilized for the three velocity components in the radial, azimuthal and streamwise directions. At the lateral, cylindrical boundary of the domain, homogeneous Neumann conditions mimicked the free-stream. Homogeneous Neumann conditions were also utilized for both pressure and eddy viscosity at all boundaries. No-slip boundary conditions were enforced on the surface of both hydrofoil and propeller by using an IB methodology. The domain was discretized using a cylindrical grid consisting of 800 × 1,026 × 2,050 (1.7 billion) points, along the radial, azimuthal and axial directions, respectively. About 160,000 and 80,000 triangles were utilized to discretize the surfaces of propeller and hydrofoil, respectively, whose Lagrangian grids were “immersed” within the Eulerian grid.

All simulations were conducted at a constant value of the Courant-Friedrichs-Lewy (CFL) number equal to 1.0, to meet the stability restrictions imposed by the three-step Runge-Kutta scheme. This condition resulted in almost 7,000 time steps for the propeller to perform each revolution. The flow was developed during two flow-through times before starting statistical sampling, with the purpose of establishing statistically steady conditions in the wake.

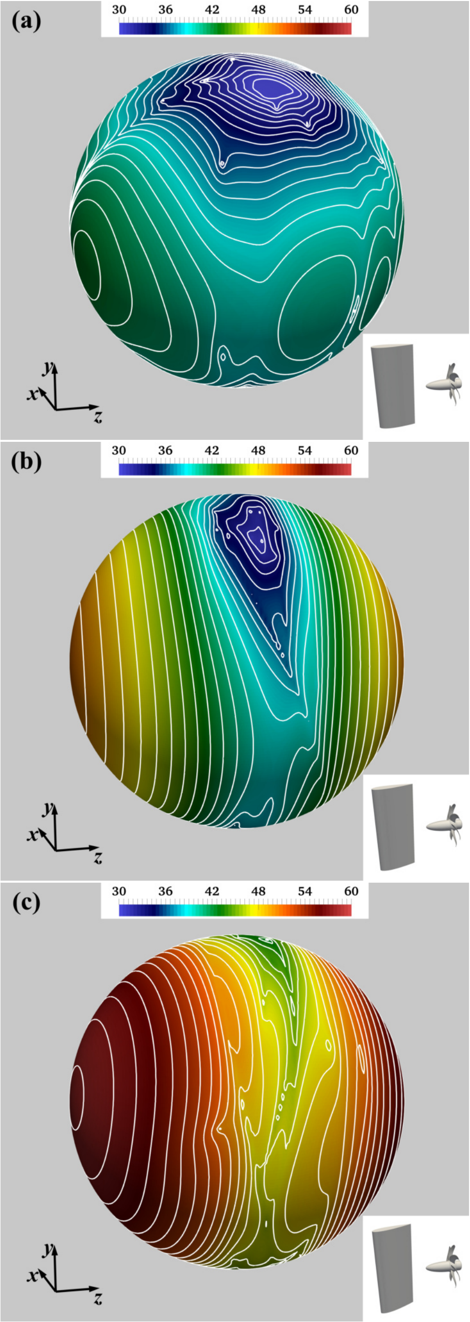

Figure 2: Distribution of the $SPLs$ in the third-octave band centered at the blade frequency over a sphere of radius $100D$, centered at the propeller: (a) *I00*; (b) *I10*; (c) *I20*. The insets showing the orientation of the hydrofoil-propeller system.

3.2 Setup of the acoustic post-processing

For the acoustic post-processing, instantaneous realizations of the solution were saved across more than 10 revolutions for each case, with a frequency equivalent to $12f_b$, where $f_b = 7n$ is the frequency of the blade passage. An overall number of 64,800 hydrophones was placed over a sphere, centered at the propeller and having a radius of $100D$, with the purpose of analyzing the directivity of the acoustic signature of the propeller. Hydrophones were equally spaced

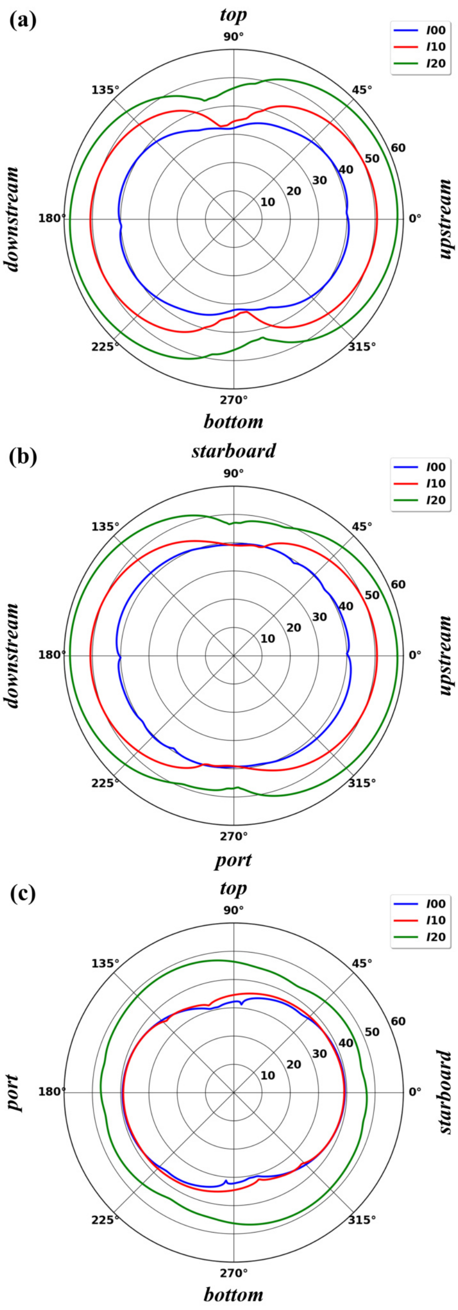

Figure 3: $SPLs$ in the third-octave band centered at the blade frequency at a distance from the propeller equal to $100D$: (a) plane $x = 0$; (b) plane $y = 0$; (c) plane $z = 0$.

of $1\,\mathrm{deg}$ in both azimuthal and polar directions. In our earlier works, we verified that the volume terms of Equation 1 are important only within a few diameters away from the axis of the propeller wake, due to vorticity and turbulence. Further away the acoustic signature is dominated by the surface integrals. The reader is referred, for instance, to the works by Posa et al (2022b) and Posa et al (2022d), where also comparisons with experiments are reported for validation. Therefore, in the present work we considered only the surface integrals of Equation 1, taking as surfaces of integration the Lagrangian grids representing the bodies immersed within the flow. This strategy allowed us also separating the sound radiated from the hydrofoil and the propeller, respectively.

We assumed as a reference the dimensional quantities of the experiments conducted by Felli & Falchi (2018), where the diameter of the propeller was $D = 0.25$ m, the advance velocity $V = 2.5$ m/s, the density of water $\rho = 998.2$ kg/m^3 and the speed of sound $c = 1,482$ m/s. Below, the results will be reported as sound pressure levels ($SPLs$) in decibels:

$$SPL = 20log_{10}\left(A_{FFT}[\widehat{p}]/\widehat{p}_0\right), \tag{6}$$

where $A_{FFT}[\widehat{p}]$ is the amplitude of the Fast Fourier Transform (FFT) of the time-history of the acoustic pressure at a particular frequency, while $\widehat{p}_0$ is a reference acoustic pressure, assumed equal to 1 μPa. Our results were post-processed further, providing them in the third-octave bands centered at three frequencies: $f = f_b$, $f = n$ and $f = 6f_b$. It is worth mentioning that, although the resolutions in space and time adopted for the present computations are very fine, to properly resolve the flow physics in the framework of LES, the hydroacoustic analysis was conducted in post-processing, relying on instantaneous realizations of the solution. Unfortunately, the frequency of time-sampling was limited by the size of the relevant files, therefore we were not able to extend the analysis of the acoustic signature to frequencies higher than $6f_b$, despite the much finer resolution in time of the present computations.

4 RESULTS

4.1 SPLs at the blade frequency

Figure 2 shows the distribution of the $SPLs$ over the sphere of hydrophones in the third-octave band centered at the blade frequency:

- The $SPLs$ are a growing function of the incidence angle of the hydrofoil.
- The highest values are achieved in the upstream and downstream directions.
- The lowest values are achieved on the propeller plane and especially in the direction aligned with the span of the hydrofoil.

These results are illustrated in better detail in Figure 3, where the three polar plots deal with the hydrophones placed on the planes of equations $x = 0$, $y = 0$ and $z = 0$, respectively.

4.2 SPLs at the shaft frequency

The $SPLs$ in the third-octave band centered at the shaft frequency are shown in Figure 4. Compared to the results at the blade frequency, both values and topology of the acoustic signature of the system are much stronger functions of the incidence of the hydrofoil. For the case ***I00***, the highest values are achieved in the direction normal to the surface of the hydrofoil. However, for increasing incidence angles the topology of the contours approaches that already seen at the blade frequency, characterized by its maxima in the

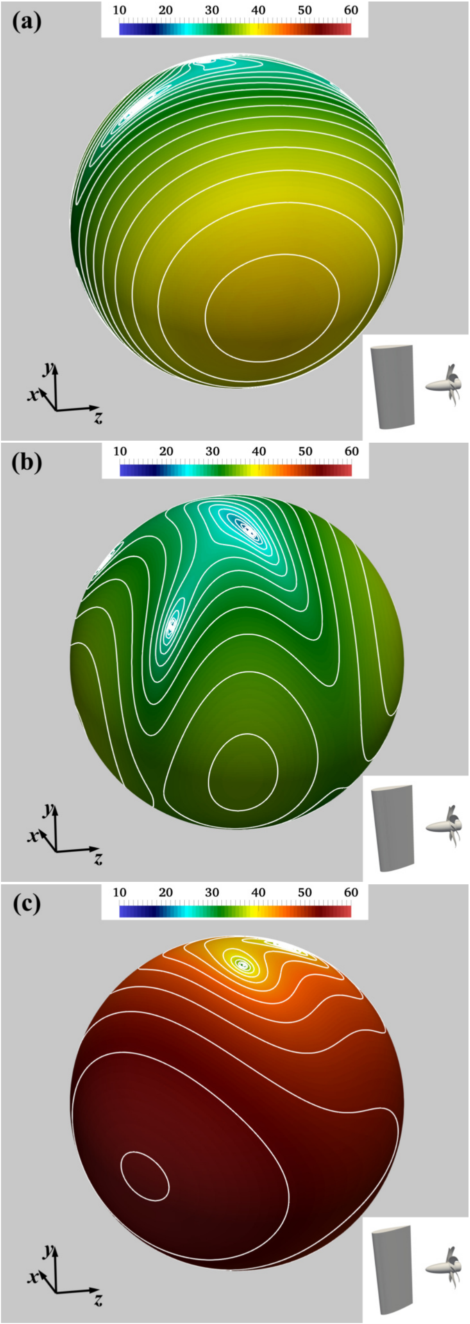

Figure 4: Distribution of the $SPLs$ in the third-octave band centered at the shaft frequency over a sphere of radius $100D$, centered at the propeller: (a) *I00*; (b) *I10*; (c) *I20*. The insets showing the orientation of the hydrofoil-propeller system.

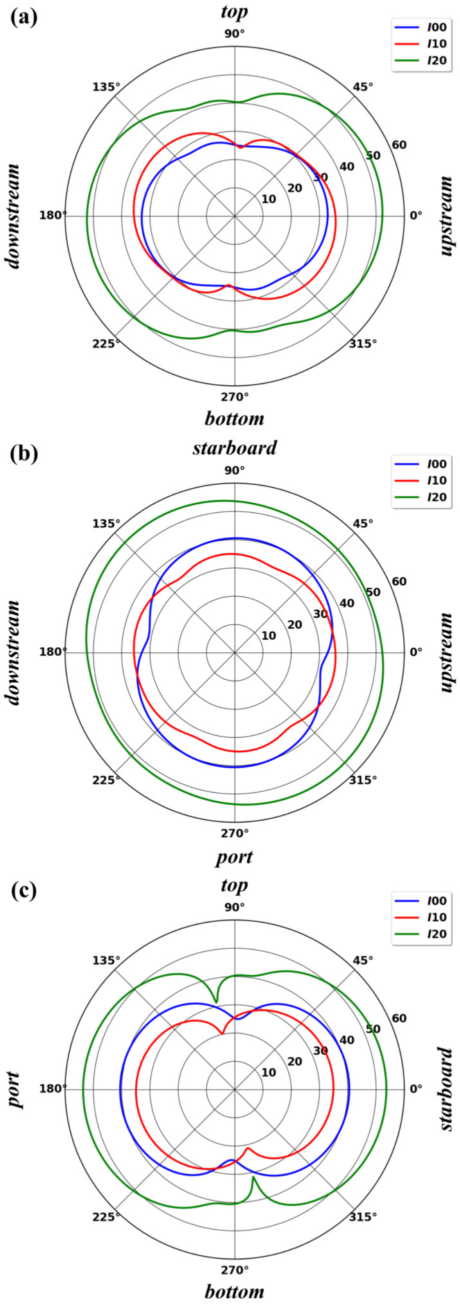

Figure 5: $SPLs$ in the third-octave band centered at the shaft frequency at a distance from the propeller equal to $100D$: (a) plane $x = 0$; (b) plane $y = 0$; (c) plane $z = 0$.

upstream and downstream directions. Again, more details about the comparison across configurations are distinguishable in Figure 5, showing the significant increase of the $SPLs$ in the case ***I20***, due to the separation affecting the suction side of the hydrofoil and the resulting impact on the working conditions of the downstream propeller.

The modification in the topology of the contours across the three panels of Figure 4 is due to the shift from an acoustic signature dominated by the hydrofoil to one dominated by the propeller, while at the blade frequency the sound coming from the propeller is always the leading one. This switch is illustrated in Figure 6, where the polar plots refer to the hydrophones in the plane $y = 0$. Interestingly, for ***I00*** the acoustic emission is dominated by the hydrofoil, especially in the x direction. However, for increasing incidence angles a significant rise of the $SPLs$ from the propeller occurs, becoming the leading ones of the overall acoustic signature.

4.3 SPLs at the frequency $f = 6f_b$

At the higher frequency $f = 6f_b$ some of the features of the acoustic signature already observed at the blade frequency are again visible, as illustrated in Figures 7 and 8. The highest $SPLs$ are achieved in the upstream and

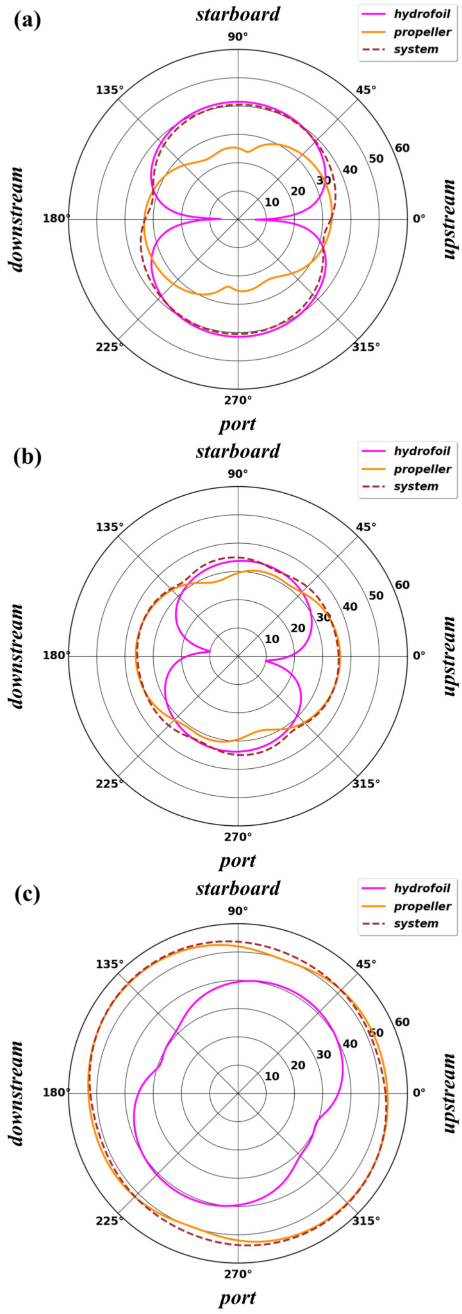

Figure 6: $SPLs$ in the third-octave band centered at the shaft frequency at a distance from the propeller equal to $100D$ on the plane $y = 0$. Comparison between hydrofoil and propeller components: (a) *I00*; (b) *I10*; (c) *I20*.

downstream directions, while the lowest ones are found on the propeller plane and especially in the spanwise direction of the hydrofoil. However, the $SPLs$ for ***I10*** are lower than those for ***I00***, maybe due to a less direct interaction between the wake of the hydrofoil and the ogive of the propeller. Nonetheless, as at the other frequencies, the highest $SPLs$ are produced at the largest incidence angle of the hydrofoil, because of the separation occurring on its suction side, increasing the loading sound coming from the propeller operating in its wake.

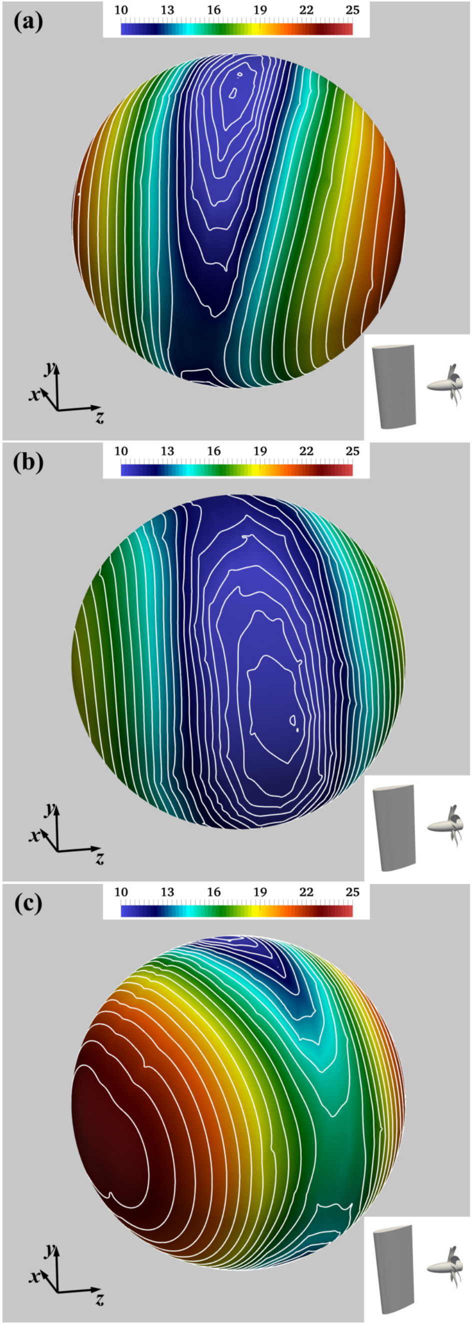

Figure 7: Distribution of the $SPLs$ in the third-octave band centered at the frequency $f = 6f_b$ over a sphere of radius $100D$, centered at the propeller: (a) *I00*; (b) *I10*; (c) *I20*. The insets showing the orientation of the hydrofoil-propeller system.

4.4 Narrow band spectra

In this section, narrow band spectra are reported, to provide a more global overview about the influence of the incidence angle of the hydrofoil on the acoustic signature. Results are provided in Figure 9 at three locations, corresponding to (a) $x/D = 100$, $y/D = 0$, $z/D = 0$ (starboard side), (b) $x/D = 0$, $y/D = 100$, $z/D = 0$ (top side) and (c) $x/D = 0$, $y/D = 0$, $z/D = 100$ (downstream side).

Figure 9(a) shows that sound at such distance from the hydrofoil-propeller system is mainly broadband, although

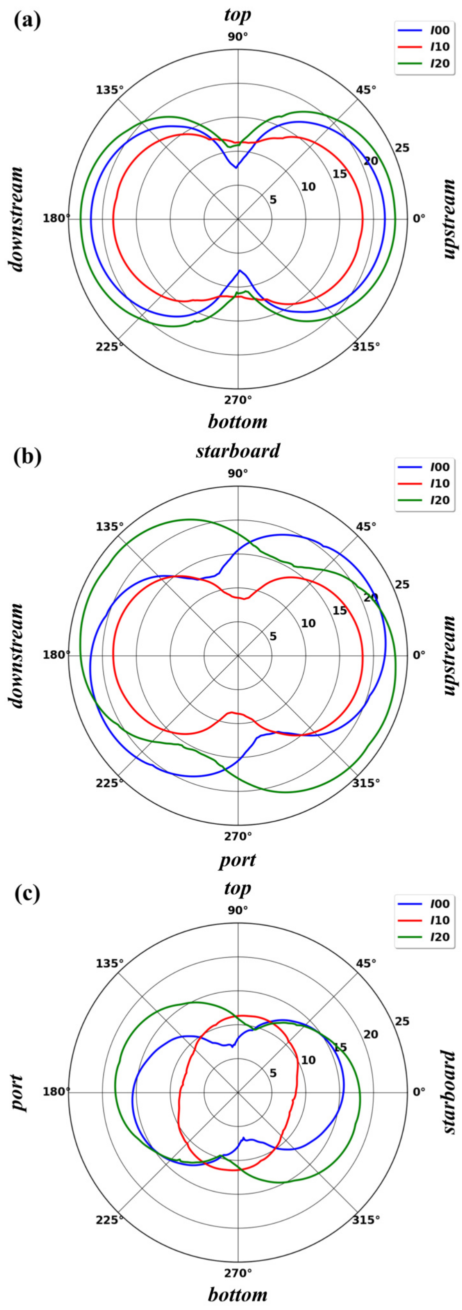

Figure 8: $SPLs$ in the third-octave band centered at the frequency $f = 6f_b$ at a distance from the propeller equal to $100D$: (a) plane $x = 0$; (b) plane $y = 0$; (c) plane $z = 0$.

both cases ***I00*** and ***I10*** still display a distinguishable peak at the blade frequency. This is not the case for ***I20***, which is however characterized by higher $SPLs$, in comparison with the conditions at smaller angles of incidence of the hydrofoil, especially in the range of the smallest frequencies of the acoustic signature.

The spectra in Figure 9(b) are similar to those in Figure 9(a), although $SPLs$ are lower, as discussed in the earlier sections of this manuscript: also at this location the tonal sound is better distinguishable for ***I00*** and ***I10***, with maxima at the blade frequency, while for ***I20*** it is broadband, achieving higher levels across all frequencies.

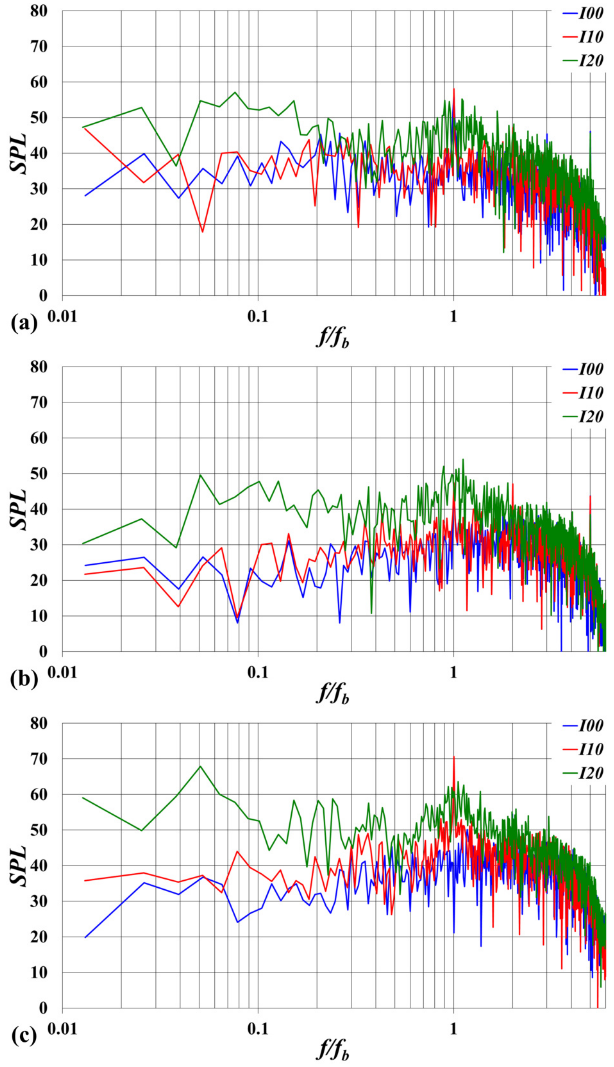

Figure 9: $SPLs$ in narrow band at hydrophones located on (a) the starboard side ($x/D = 100$; $y/D = 0$; $z/D = 0$), (b) the top side ($x/D = 0$; $y/D = 100$; $z/D = 0$) and (c) the downstream side ($x/D = 0$; $y/D = 0$; $z/D = 100$).

In Figure 9(c), dealing with the hydrophone placed downstream of the system, $SPLs$ are higher than in the other panels of the same figure. In this case also ***I00*** does not display any peak at the blade frequency, in contrast with ***I10***. Once again, the most obvious rise in $SPLs$ for the configuration ***I20*** occurs at the lowest frequencies of the acoustic signature, although well evident across all available frequencies.

In Figure 10 additional narrow band spectra are shown, with the purpose of providing further evidence of the accuracy of the approach. In the vicinity of the hydrofoil-propeller system, where compressibility effects can be neglected, the spectra of the acoustic pressure from FWH and those of hydrodynamic pressure from LES are expected to be similar, while moving further away deviations become increasingly more distinguishable. It is worth mentioning that the results reported in Figure 10 deal with our earlier work discussed in Posa et al (2022b), where the acoustic near field was studied. It should be noted that in that case

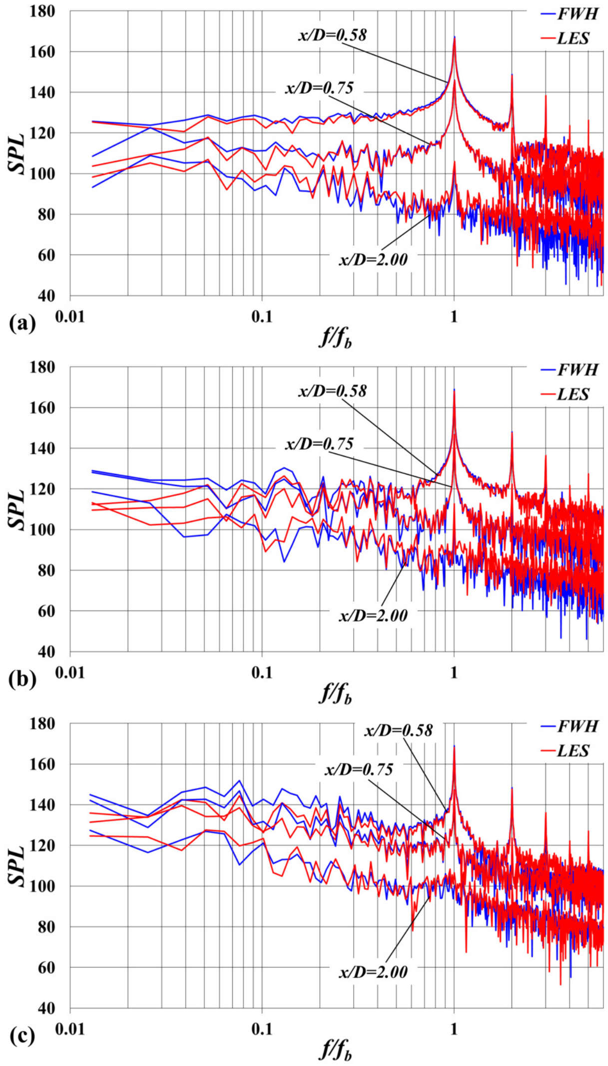

Figure 10: $SPLs$ in narrow band at hydrophones located at the coordinates $x/D = 0.58, 0.75, 2.00$, $y/D = 0.0$ and $z/D = 0.0$ for the configurations (a) *I00*, (b) *I10* and (c) *I20*: comparison between the spectra of hydroacoustic pressure from FWH and those of hydrodynamic pressure from LES.

the contribution of the quadrupole component of the acoustic pressure was included, since it is important in the vicinity of the source and definitely not negligible, if compared with the linear component.

The three panels of Figure 10 deal with the cases ***I00***, ***I10*** and ***I20***, respectively. For each case hydrophones placed at the coordinates $y/D = 0.0$ and $z/D = 0.0$ are considered, at locations on the starboard side corresponding to $x/D = 0.58$, $x/D = 0.75$ and $x/D = 2.00$, respectively. For all cases of incidence of the hydrofoil the agreement between FWH and LES is very close across the whole range of frequencies. This is especially evident at the tonal frequencies. These results are consistent with the expected ones and provide additional confidence about the accuracy of the approach adopted in the present study.

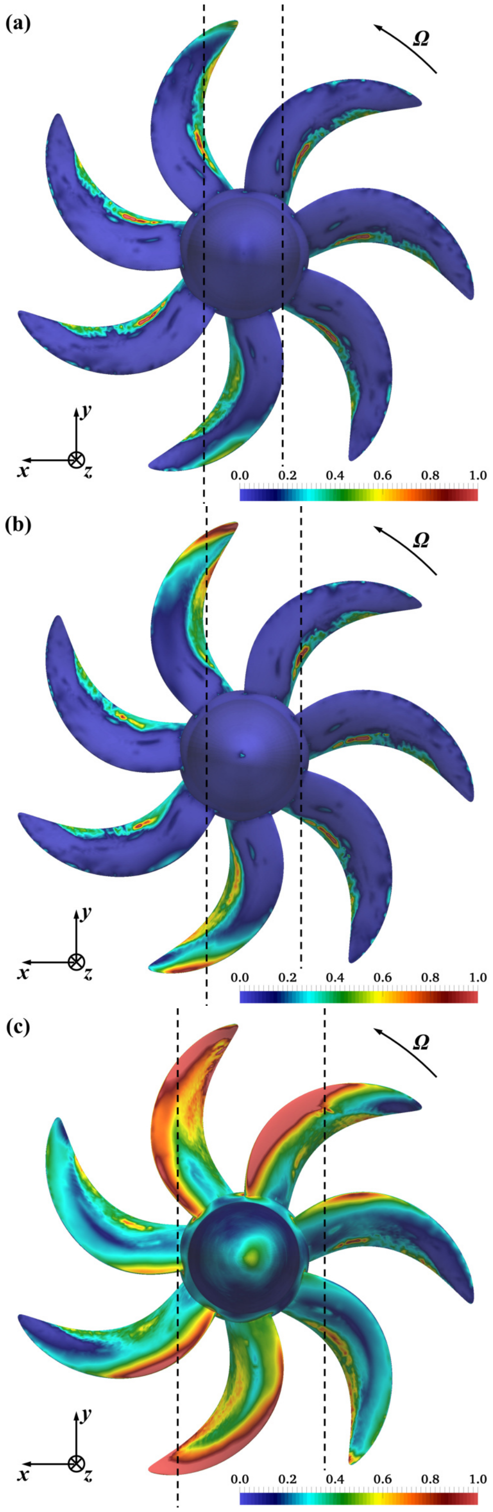

Figure 11: Root-mean-squares of the phase-averaged fluctuations in time of the pressure coefficient at a distance of $0.005D$ from the suction side of the propeller blades: (a) *I00*; (b) *I10*; (c) *I20*. Dashed lines for the projection of the hydrofoil on the propeller plane.

4.5 Pressure fluctuations on the propeller

We verified that the leading source of sound is the loading component from the propeller, tied to the fluctuations of hydrodynamic pressure on its surface. Figures 11 and 12 show the contours of the root-mean-squares in time of

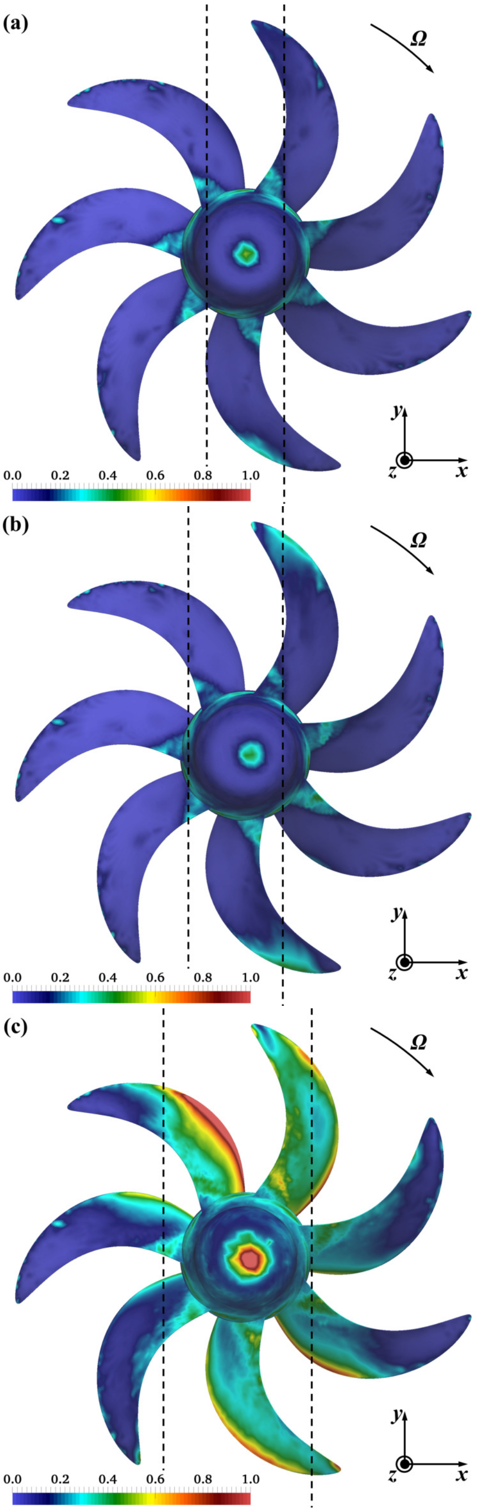

Figure 12: Root-mean-squares of the phase-averaged fluctuations in time of the pressure coefficient at a distance of $0.005D$ from the pressure side of the propeller blades: (a) *I00*; (b) *I10*; (c) *I20*. Dashed lines for the projection of the hydrofoil on the propeller plane.

the pressure coefficient on the suction and pressure sides of the propeller blades, respectively. Fluctuations were computed as phase-averaged statistics, by considering instantaneous realizations of the solution corresponding to the particular position of the propeller blades of Figures 11 and 12. This strategy allowed us isolating the effect of the wake of the hydrofoil on the blades placed within its wake, showing the rise of the pressure fluctuations, compared to the other blades. The pressure coefficient was defined as $c_p = (p - P)/(0.5\rho V^2)$, where p is the local hydrodynamic pressure and P its free-stream value. The dramatic increase of the pressure fluctuations in the case ***I20*** is evident, especially for the blades operating in the wake of the hydrofoil. This is due to the separation phenomena affecting its suction side, promoting a substantial increase of the turbulence levels ingested by the propeller. This is the case not only for the suction side of the propeller blades (see Figure 11), facing the hydrofoil, but also for their pressure side (see Figure 12).

5 CONCLUSIONS

Results of Large Eddy Simulations on a hydrofoil-propeller system were utilized to reconstruct in post-processing its acoustic signature, by using the Ffowcs-Williams & Hawkings acoustic analogy. The acoustic pressure was computed on a sphere of 64,800 hydrophones centered at the propeller, having a radius of 100 propeller diameters. This study revealed the significant impact of the separation occurring on the suction side of the hydrofoil at large angles of incidence, increasing the loading component of the sound coming from the surface of the propeller operating in its wake. The highest sound pressure levels were achieved in the upstream and downstream directions. The lowest ones occurred on the plane of the propeller, with minima placed in the spanwise direction of the hydrofoil. Interestingly, at low frequencies the sound from the upstream hydrofoil at zero incidence was higher than that from the propeller, achieving its highest values on the port and starboard sides. However, for increasing incidence angles the acoustic signature of the system was largely dominated by the propeller, because of the stronger disturbance of its inflow conditions.

REFERENCES

Balaras, E. (2004). ‘Modeling complex boundaries using an external force field on fixed Cartesian grids in large-eddy simulations’. Computers & Fluids **33**(3), pp. 375–404.

Bensow, R. & Liefvendahl, M. (2016). ‘An acoustic analogy and scale-resolving flow simulation methodology for the prediction of propeller radiated noise’. Proceedings of the 31st Symposium on Naval Hydrodynamics, Monterey, California, USA.

Chou, E., Southall, B.L., Robards, M. & Rosenbaum, H.C. (2021). ‘International policy, recommendations, actions and mitigation efforts of anthropogenic underwater noise’. Ocean & Coastal Management **202**, p. 105427.

Cianferra, M., Petronio, A. & Armenio, V. (2019). ‘Non-linear noise from a ship propeller in open sea condition’. Ocean Engineering **191**, p. 106474.

Di Francescantonio, P. (1997). ‘A new boundary integral formulation for the prediction of sound radiation’. Journal of Sound and Vibration **202**(4), pp. 491–509.

Felli, M. & Falchi, M. (2018). 'A parametric survey of propeller wake instability mechanisms by detailed flow measurement and time resolved visualizations'. Proceedings of the 32nd Symposium on Naval Hydrodynamics, Hamburg, Germany.

Ffowcs-Williams, J.E. & Hawkings, D.L. (1969). 'Sound generation by turbulence and surfaces in arbitrary motion'. Philosophical Transactions of the Royal Society of London. Series A, Mathematical and Physical Sciences **264**(1151), pp. 321–342.

Ge, M., Svennberg, U. & Bensow, R.E. (2022). 'Investigations on prediction of ship noise using the FWH acoustic analogy with incompressible flow input'. Ocean Engineering **257**, p. 111531.

Kimmerl, J., Mertes, P. & Abdel-Maksoud, M. (2021). 'Application of large eddy simulation to predict underwater noise of marine propulsors. Part 2: Noise generation'. Journal of Marine Science and Engineering **9**(7), p. 778.

Kimmerl, J. & Abdel-Maksoud, M. (2023). 'Visualization of Underwater Radiated Noise in the Near-and Far-Field of a Propeller-Hull Configuration Using CFD Simulation Results'. Journal of Marine Science and Engineering **11**(4), p. 834.

Lidtke, A.K., Lloyd, T., Lafeber, F.H. & Bosschers, J. (2022). 'Predicting cavitating propeller noise in off-design conditions using scale-resolving CFD simulations'. Ocean Engineering **254**, p. 111176.

Lighthill, M.J. (1952). 'On sound generated aerodynamically I. General theory'. Proceedings of the Royal Society of London. Series A. Mathematical and Physical Sciences **211**(1107), pp. 564–587.

Nicoud, F. & Ducros, F. (1999). 'Subgrid-scale stress modelling based on the square of the velocity gradient tensor'. Flow, turbulence and Combustion **62**(3), pp. 183–200.

Posa, A., Broglia, R., Felli, M., Falchi, M. & Balaras, E. (2019). 'Characterization of the wake of a submarine propeller via large-eddy simulation'. Computers & Fluids **184**, pp. 138–152.

Posa, A., Broglia, R., Felli, M., Cianferra, M. & Armenio, V. (2022a). 'Hydroacoustic analysis of a marine propeller using large-eddy simulation and acoustic analogy'. Journal of Fluid Mechanics **947**, p. A46.

Posa, A., Felli, M. & Broglia, R. (2022b). 'Influence of an upstream hydrofoil on the acoustic signature of a propeller'. Physics of Fluids **34**(4), p. 045112.

Posa, A., Broglia, R. & Balaras, E. (2022c). 'The dynamics of the tip and hub vortices shed by a propeller: Eulerian and Lagrangian approaches'. Computers & Fluids **236**, p. 105313.

Posa, A., Broglia, R. & Felli, M. (2022d). 'Acoustic signature of a propeller operating upstream of a hydrofoil'. Physics of Fluids **34**(6), p. 065132.

Posa, A., Broglia, R., Balaras, E. & Felli, M. (2023a). 'The acoustic signature of a propeller-hydrofoil system in the far field'. Physics of Fluids **35**(7), p. 075101.

Posa, A., Felli, M. & Broglia, R. (2023b). 'Acoustic far field of a propeller working in the wake of a hydrofoil'. Physics of Fluids **35**(12), p. 125121.

Sezen, S. & Atlar, M. (2022). 'Numerical investigation into the effects of tip vortex cavitation on propeller underwater radiated noise (URN) using a hybrid CFD method'. Ocean Engineering **266**, p. 112658.

Stark, C. & Shi, W. (2021). 'Hydroacoustic and hydrodynamic investigation of bio-inspired leading-edge tubercles on marine-ducted thrusters'. Royal Society open science **8**(9), p. 210402.